Structural characteristics of methylsilsesquioxane based porous low-*k* thin films fabricated with increasing cross-linked particle porogen loading

Hae-Jeong Lee, Christopher L. Soles,[a] Da-Wei Liu, Barry J. Bauer, Eric K. Lin, and Wen-Li Wu
Polymers Division, National Institute of Standards and Technology, Gaithersburg, Maryland 20899

Michael Gallagher
Rohm and Haas Company, Marlborough, Massachusetts 0175

(Received 18 January 2006; accepted 20 July 2006; published online 21 September 2006)

Methylsilsesquioxane (MSQ) based porous low-*k* dielectric films are characterized by x-ray porosimetry (XRP) to determine their pore size distribution, average density, wall density, and porosity. By varying the porogen content from 1% to 30% by mass, the porosity changes from 12% to 34% by volume, indicating that the base MSQ matrix material contains approximately 10% by volume inherent microporosity. The wall density of this matrix material is measured to be 1.33–1.35 g/cm^3, independent of porosity. The average pore radii determined from the XRP adsorption isotherms increase from 6 to 27 Å with increased porogen loadings. Small angle neutron scattering measurements confirm these XRP average pore radii for the films with porogen loading higher than 10% by mass. © *2006 American Institute of Physics*. [DOI: 10.1063/1.2337772]

INTRODUCTION

With the minimum feature size on the typical integrated circuit (IC) predicted to approach 50 nm by 2009, the device performance will be highly susceptible to increases in propagation delay, cross-talk noise, and power dissipation of the interconnect structure. These parasitic effects, however, can be minimized by introducing lower resistivity metals in the conduction lines and/or lower dielectric constant (low-*k*) insulating materials. Over the past several years, there has been a tremendous amount of research on low-*k* films and several classes of materials have emerged. Candidate materials include organic polymers, fluorinated silicates, inorganic-organic hybrids, and several types of porous materials.[1–9] There is a consensus in the semiconductor industry that the requirements for future devices can only be achieved by using ultra low-*k* materials with dielectric constants less than 2.4, even though the target date has recently been pushed back according to the 2004 edition of International Technology Roadmap for Semiconductors (ITRS).[10] In short, highly porous materials are needed for low-*k* interlevel dielectrics in future IC chips since the target values cannot be obtained with fully dense materials.

Among the candidate material classes, methylsilsesquioxane (MSQ) based porous materials have received significant attention. The neat MSQ matrix material, a silicon-oxygen network with methyl side groups, is hydrophobic (water uptakes $<1\%$ by mass) and typically exhibits a dielectric constant between 2.7 and 2.9. Inducing porosity can decrease this dielectric constant further, but the added porosity can also adversely affect other properties essential to chip integration and performance such as mechanical strength, electrical properties, and Cu diffusion through the insulator.[11] Improving these properties with respect to how the low-*k* material withstands the subsequent processing steps, such as etching, cleaning, ashing, and chemical mechanical polishing, is one of the greatest challenges facing future IC chip fabrication. It is vital to characterize the on-wafer structure of these porous thin films in order to optimize the processing conditions to obtain the desired porous structures. More generally, controlling the pore size and shape is of great interest not only for low-*k* materials but also for areas using porous thin films such as catalysts, photonic materials, and sensor applications.[12]

Gas adsorption, mercury intrusion, and quartz crystal microbalances are commonly used to characterize the specific area, pore volume, and pore size distribution (PSD) of porous materials. However, porous low-*k* thin films for semiconductor IC chip have four orders of magnitude smaller sample volume than those of the porous materials for the other application.[13] Conventional characterization methods lack the sensitivity to be applied to low-*k* dielectric films. Furthermore, the porous low-*k* films less than 1 μm thick are usually deposited on a 1 mm thick silicon substrate. Currently, there are only a few methodologies suitable to investigate the pore structure in low-*k* films, including focused positron beam techniques,[14,15] ellipsometry porosimetry (EP),[16] small angle x-ray scattering (SAXS),[17] and a combination of specular x-ray reflectivity (SXR), small angle neutron scattering (SANS), and ion-beam scattering.[18] For the later technique SANS can be replaced by SAXS and the information obtained are identical. However, there are inherent limitations to each of these methodologies. The positron beam technique is well suited for small pores, less than 20 Å, also requires a high vacuum environment. EP assumes that the optical polarizability of adsorbate and adsorbent is additive in the nanopores. Both SAXS and SANS lack the sensitivity for pores smaller than 5 Å in diameter.

Recently, we have developed x-ray porosimetry (XRP)

[a]Author to whom correspondence should be addressed; electronic mail: csoles@nist.gov

to characterize the pore structures of low-k thin films using SXR.[19,20] Like classic porosimetry techniques, XRP also deduces the PSD from the uptake of probe molecules inside the pores as the partial pressure of the adsorbate is varied. For thin films supported on thick silicon substrates, the probe molecule uptake is measured directly from the change in the electron density of the film upon adsorption. In this work, we apply XRP to spin-on porous MSQ films with micropores in the wall material and mesopores generated by the removal of a porogen.[21,22] The effects of porogen loading on the pore structure are investigated by varying the porogen loading from 1% to 30% by mass. We report critical structural characteristics such as porosity, PSD, average film density, and the matrix material or wall density. The results from XRP are compared with the more established combination of SANS and SXR described elsewhere.[18]

EXPERIMENTAL SECTION

Cross-linked polymeric particles for the porogen template were prepared by a gradual addition of polymerization of a mixture of acrylate and methacrylate monomers, described previously in the literature.[22] Solutions were then prepared by mixing the MSQ resin with the cross-linked polymer particles at loadings of 1%, 5%, 10%, 20%, and 30% by mass into propyleneglycolmonomethylether. The solutions were spin cast at 209 rad/s (2000 rpm) into films on 200 mm diameter silicon wafers and sequentially baked at 90 and 150 °C (for 1 min at each temperature) in air before being sealed in a quartz furnace under nitrogen. This furnace was ramped to 450 °C at 10 °C/min and held at 450 °C for 1 h to remove the porogen template. The elemental composition of the cured films was determined through a combination of Rutherford, grazing angle forward, and forward recoil ion-beam scatterings.[23]

The SXR measurements were accomplished on a modified high-resolution x-ray diffractometer in a θ-2θ configuration at the specular conditions with the incident angle equal to the detector angle. A finely focused Cu $K\alpha$ xray source with a wavelength λ of 1.54 Å was conditioned with a four-bounce germanium (220) monochromator and focused onto the film of interest. A three-bounce germanium (220) channel cut crystal was also used to direct the reflected x rays into the detector. The sample and detector goniometer have an active servofeedback system to provide an angular reproducibility of ±0.0001°.[24] Typically the specular reflected intensity was collected as a function of incident angle between 0.1° and 1.0°.

The gaseous probe or adsorbate molecule in this work was toluene. The partial pressure is defined as the actual vapor pressure of the toluene divided by the saturated or equilibrium vapor pressure at the same temperature of the sample. The volume fraction of toluene adsorption is directly determined from the critical angle for total x-ray reflection. The Kelvin equation will be used to calculate the relationship between the partial pressure of the gas and the critical pore size for condensation. Note that the Kelvin equation is the simplest approach to relate pore size and partial pressure based on the mechanism of capillary condensation. If, for a given system, the mechanism of pore filling is not simple capillary condensation, the Kelvin equation should be replaced with a more appropriate expression. Nevertheless, the selected example will illustrate how very detailed PSD information can be obtained with XRP.

Each low-k film was mounted in the reflectometer, conditioned at 175 °C in vacuum for 2 h, and then cooled to room temperature. While still under vacuum reflectivity was collected to determine the critical angle of the evacuated sample. Then a stream of air that has been saturated with toluene vapor at (20±0.1) °C by slowly bubbling the air through the liquid toluene is passed over the sample. When the sample is also at 20 °C ($P/P_0=1$), toluene fully condenses in all the available pores. The effective partial pressure of the environment was varied by gradually increasing and decreasing the sample temperatures between 20 and 125 °C, while the temperature of the air saturated with toluene was kept at 20 °C. After each temperature change, 30 min was allowed for thermal equilibration before the ensuing reflectivity data were collected. From our experience toluene is an excellent vapor for probing the porosity of MSQ-type films. Apparently toluene molecules are able to permeate through the matrix material and therefore access all the pores. First, a drop of liquid toluene will readily wet the surface of a MSQ-type film, including those studied here. Second, a very slight swelling of the film thickness, on the order of 1%, occurs in the presence of the saturated toluene vapor. For these reasons we are confident that toluene can make its way into all of the micro- or mesopores of the film. Only those pores physically smaller than a toluene molecule would seem to be inaccessible.

Complementary SANS measurements were performed on the 8 m NG1 beamline at the National Institute of Standards and Technology Center for Neutron Research. The neutron wavelength λ was 6 Å with a wavelength spread [full width at half maximum (FWHM)] $\Delta\lambda/\lambda$ of 0.14. The sample to detector distance was 3.6 m and the detector was offset by 3.5° from the incident beam to increase the range of detection angles. 10 pieces of each low-k film were stacked together and placed in a windowless sample holder under vacuum to increase the signal to noise ratio in the scattering. Under these conditions approximately 6 h was required to obtain a two-dimensional scattering pattern with sufficient statistics. The circularly averaged two-dimensional data were corrected and reduced using standard reduction methods.[18]

RESULTS AND DISCUSSION

Figure 1 shows experimental SXR data at 20 °C for the porous low-k films of varying porogen contents both under vacuum and in the saturated toluene atmosphere. The reflectivity data are presented as the logarithm of the reflectivity R ($R=I_{\text{reflected}}/I_{\text{incident}}$, where I is the beam intensity) as a function of q [$q=(4\pi/\lambda)\sin\theta$, where θ is the incident and reflected angles of the x rays]. The incident x rays begin to penetrate the films at a critical value of q, resulting in a sharp drop in the reflected intensity. This critical angle is determined by fitting the SXR curves using a least-squares fitting routine based on the algorithm of Parratt.[25] The square of the

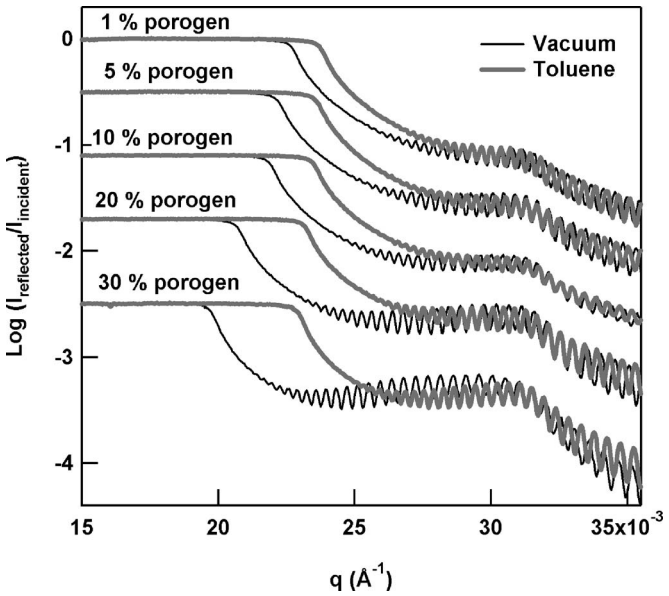

FIG. 1. The SXR curves of the MSQ based porous low-k thin films are displayed as a function of increasing porogen content. The data are presented as the logarithm of the ratio of the reflected ($I_{\text{reflected}}$) to the incident (I_{incident}) xray intensities vs the magnitude of the scatting vector q in the film thickness direction. The black and gray curves indicate the experimental data taken under vacuum and in the saturated toluene atmosphere, respectively. The data have been vertically offset for clarity. The standard uncertainty in the reflectivity is less than the linewidth.

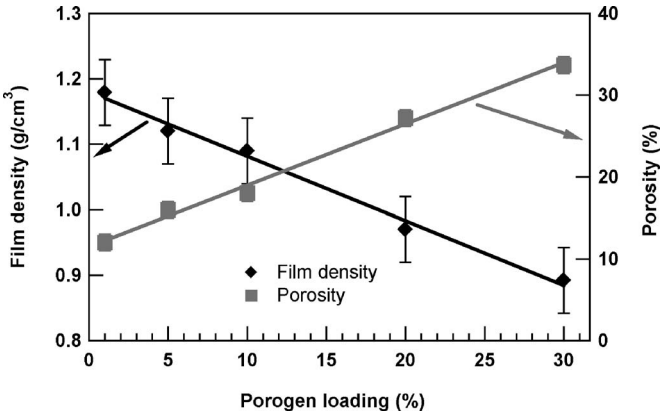

FIG. 2. The variations of the average film density and porosity are shown as the porogen content increases from 1% to 30% by mass. The black and gray lines are linear fits of film density and porosity as a function of porogen loading, respectively.

critical angle, q_c^2, in unit of Å^{-2} is related to the density of the film through the equation $q_c^2 = 16\pi r_e \rho_e$, where ρ_e is the electron density and r_e is the classical electron radius. The atomic compositions to convert ρ_e into a mass density are summarized in Table I.

Comparing the reflectivity curves from the samples under vacuum, Fig. 1 demonstrates that the film density decreases with increasing porogen content; the critical angle for total reflection shifts to lower q (lower θ) with increasing porogen. It is also evident that for each film the critical angle shifts to higher q in the presence of the saturated toluene vapor. This results from capillary condensation of the toluene inside the accessible pores. A larger difference between critical angles of the vacuum and the toluene-saturated curves indicates a larger uptake of toluene, and thus a greater porosity. From the vacuum and toluene-saturated curves one can calculate the total amount of toluene adsorbed, i.e., the total porosity, and the density of the wall material separating the pores through the following two equations: $\rho_{\text{av}} = \rho_w(1-P)$ and $\rho_{\text{av,toluene}} = \rho_w(1-P) + \rho_{\text{toluene}}P$. Here, ρ_{av}, ρ_w, P, $\rho_{\text{av,toluene}}$, and ρ_{toluene} are the average density of the film in vacuum, the density of the wall material between the pores, the porosity of the film, the average density of porous thin film saturated under toluene vapor, and the average density of the condensed toluene (0.865 g/cm^3 at 20 °C), respectively. It is important to realize that ρ_w calculated by this method is an average of the wall material plus any unfilled pores that are too small or inaccessible to the toluene molecules.

The structural characteristics including wall density, porosity, and average density of the different films are summarized in Table I. Figure 2 indicates a linear dependence of ρ_{av} and P on the porogen loading; the film density decreases and porosity increases with increasing porogen. In detail, the porosities of the films are 12%, 16%, 18%, 27%, and 34% by volume for the porogen loadings of 1%, 5%, 10%, 20%, and 30% by mass, respectively. It is interesting that the film with a porogen content of 1% has a porosity of 12%. Extrapolat-

TABLE I. Structural properties of MSQ based porous low-k thin films fabricated with varying porogen loading contents. The relative standard uncertainties of the atomic composition, q_c^2, density, porosity, and pore radius are ±5%, 500 Å^{-2}, 0.05 g/cm^3, 1%, and 1 Å, respectively.

Porogen loading contents (%)	Atomic composition (C:O:Si:H) (%)	q_c^2 (E-4) (Å^{-2})	Average density (g/cm^3)	Wall density (g/cm^3)	Porosity (%)	Pore radius (Å)		
						XRP		SANS
						Ads.[a]	Des.[a]	Low q
1	20:24:16:40	5.21	1.18	1.34	12	*6*	*5*	*2*
5	18:23:15:44	4.98	1.12	1.34	16	Not measured		
10	17:22:15:46	4.86	1.09	1.33	18	*10*	11	9
20	17:21:13:49	4.35	0.97	1.34	27	*18*	14	*16*
30	19:25:15:41	3.95	0.89	1.35	34	*27*	16	*27*

[a]The columns denoted by "Ads." and "Des." indicate the pore radius determined from the adsorption and desorption isotherms, respectively.

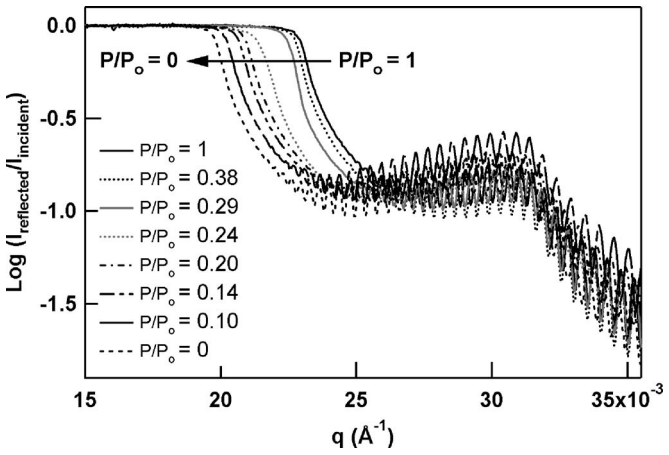

FIG. 3. Changes in the SXR curves are shown as the toluene partial pressure decreases from 1 to 0 for the MSQ film with a 30% porogen loading. The standard uncertainty in the reflectivity is less than the line width.

ing the linear dependence to 0% porogen content yields a porosity of approximately 11%. This would seem to indicate an intrinsic porosity of the neat MSQ material, regardless of porogen loading. While porogen-free sample was not available for experimental corroboration, we have observed such intrinsic porosity in similar MSQ-type materials. Notice that the porogen loading is given in percent by mass while the porosity is given in percent by volume. Since the mass density of the pure porogen is unknown, we assume that the mass and volume fractions of the porogen are equal. This assumption is reasonable given that the porogen is polymeric and the density of most polymers, either semicrystalline or amorphous, ranges from 1.0 to 1.35 g/cm^3. Given the nearly constant ρ_w of 1.35 g/cm^3 observed here, the potential error in assuming that the mass loading of the porogen equals the volume loading is approximately 0%–35%, i.e., 1% by mass porogen loading might be equal to 1%–1.35% in terms of volume. This is not a significantly large difference.

Assuming an intrinsic 11% volume porosity of MSQ wall material in all the samples our results suggest that the porogen generates approximately 1%, 4%, 7%, 15%, and 23% volume porosities for porogen loadings of 1%, 5%, 10%, 20%, and 30% by mass, respectively. The conversion of porogen to void volume does not seem to be conserved. This is also supported by the slope of 0.75 for the dependence of P on the porogen loading in Fig. 2; a slope of unity would indicate a complete volume conversion. It is possible that diffusion barriers form around the pore as it is formed and not all of the decomposition products escape the film.[26] Likewise, there could also be a pore collapse or coalescence mechanism at high temperature slightly reducing the final porosity.

Figure 3 displays a series of reflectivity curves as a function of toluene partial pressure for the 30% by mass porogen-loaded film. In this example the critical angle shifts to lower values as the partial pressure P/P_0 decreases from 1 to 0, generated by the desorption of the toluene. The biggest change in the critical angle occurs in the partial pressure range from 0.2 to 0.3, indicating that a large fraction of pores are drained in this partial pressure range. Because the density

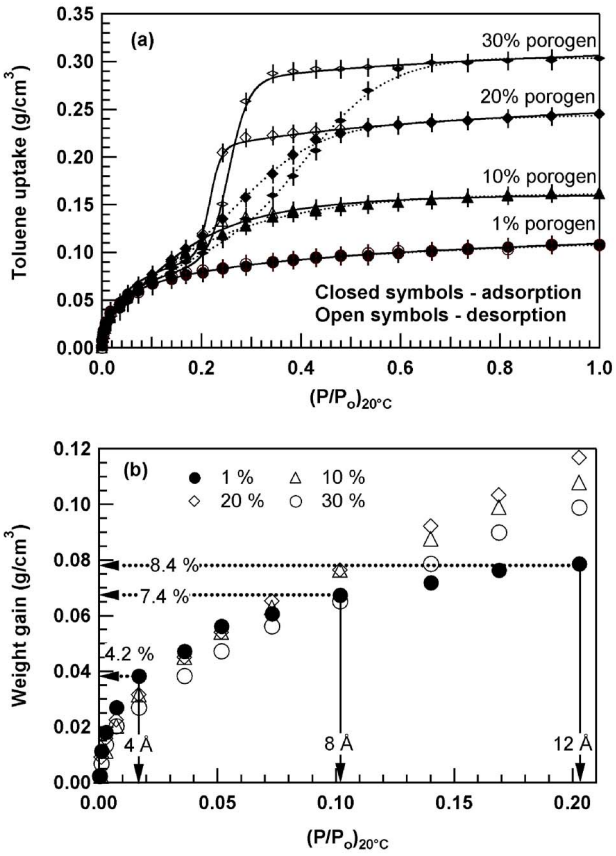

FIG. 4. (a) the complete adsorption and desorption isotherms for all of the different porogen loadings into the MSQ films. The lines are arbitrary smooth fits, using the sum of a sigmoidal and a log normal function. (b) enlarges just the adsorption branch of the isotherms at low partial pressures to reveal a greater detail in the region of micropore filling.

of liquid toluene is known, these changes in the critical angle can be converted in the amount of toluene adsorbed or evaporated. The adsorption and desorption isotherms in Fig. 4 show how much toluene is adsorbed or evaporated as a function of increasing or decreasing the partial pressure.

The 1% porogen films display a prominent toluene uptake at low partial pressures and quickly level off. There is also no hysteresis between the adsorption and desorption branches. This is characteristic of micropores, i.e., pores that are less than 1 nm in radius.[27,28] These micropores are the inherent porosity of the MSQ matrix. Figure 4(b) expands the adsorption data from part (a) in the lower partial pressure range of micropore filling; the desorption data and smooth fits are removed for clarity. At the beginning of the uptake in 1% porogen sample, a pronounced adsorption progresses up to a partial pressure of 0.02, with moderate adsorption up to 0.10. It is notable that the film with 1% porogen actually adsorbs more toluene than the film with 30% porogen up to a partial pressure of 0.05. This is consistent with the fact that the micropores are inherent to the wall material, not the porogen, and the 1% porogen film has the largest fraction of wall material.

At each partial pressure there is a critical radius for capillary condensation that reveals information about the pore radii. The Kelvin equation predicts the critical pore radius r_c for capillary condensation or evaporation through

$$r_c = -\frac{2V_m\gamma}{RT}\frac{1}{\ln(P/P_0)}, \quad (1)$$

where γ is the liquid surface tension, V_m is the molar volume of the liquid, P is the vapor pressure, and P_0 is the equilibrium vapor pressure at temperature T. From this relationship one can determine the porosity as a function of pore size. For example, a partial pressure of 0.1 corresponds to a radius of 8 Å and for the film with 1% porogen approximately 7.4% out of the total 12% porosity is already filled; 7.4% of the pores appear to have radii smaller than 8 Å. Beyond a partial pressure of 0.10 the adsorption proceeds gradually to fill the larger pores larger than 8 Å, accounting for approximately 1/3 of total porosity.

The films with higher porogen content adsorb toluene over a broader range of partial pressures. At low partial pressures the adsorption in the films with 20% and 30% porogen contents is gradual at first, but increases steeply at intermediate partial pressures due to the capillary condensation in mesopores. After these mesopores are filled, the adsorption isotherms level off. Note that capillary condensation and evaporation do not take place at the same partial pressures, i.e., there is an appreciable hysteresis loop. The hysteresis loop is highly asymmetric (broad on adsorption, narrow on desorption), suggesting that pore connectivity (network) effects are important.[27] If larger pores can only be accessed through the "bottlenecks" of surrounding smaller pores, the larger pores are not free to desorb at the relative pressure corresponding to their critical capillary radius. These smaller pores must desorb first before the toluene can escape the larger pores. This result is a simultaneous draining of both the small and large mesopores at a partial pressure corresponding to the critical radius of the smaller pores. In Fig. 4 most of the desorption for the films with 20% and 30% porogen occurs sharply in the narrow partial pressure range from 0.2 to 0.3. This apparently corresponds to the simultaneous draining of the large and small mesopores. These types of pore blocking effects are well documented in the porosimetry literature.[29]

Quantitative PSDs can be obtained from the data in Fig. 4 by using Eq. (1) to convert the partial pressure axis to a pore radius and essentially taking the derivative of the isotherms as a function of radius. This distribution can be taken directly from a point-by-point differentiation of the experimental porosimetry data, but typically results in noisy PSDs; scatter in the toluene uptake values is magnified through the differentiation. To obtain smooth PSDs we recommend fitting the uptake data in Fig. 4 with smooth, empirical fitting functions. Examples of arbitrary fit functions that adequately parametrize the uptake data are shown in Fig. 4(a). The analytical form of the fit function is of little form as long as the function accurately represents the experimental data. When the differentiation is applied to the smooth fit function the result is a smooth, reasonable PSD. The PSDs from the adsorption and desorption isotherms in Fig. 4(a) are shown in Figs. 5(a) and 5(b), respectively.

As expected, the adsorption pathways display a broad distribution of pore sizes and a larger average pore size in comparison to the desorption branch. Pores nearly as large as

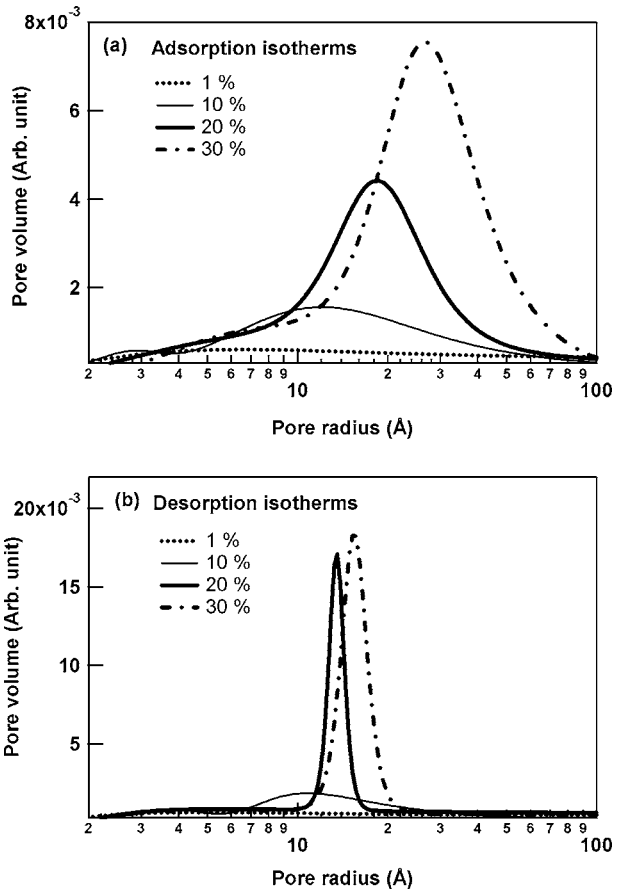

FIG. 5. Pore size distributions generated from the smooth fits to the data in Fig. 4. (a) and (b) correspond to the adsorption and desorption isotherms, respectively.

100 Å are evidenced on the adsorption branch for the samples with 20% and 30% porogen while the corresponding desorption data show a narrow distribution of pores in the 10–25 Å range. This reflects the classic connectivity or bottleneck effects described above. 10–25 Å appear to be the radii of the small pores that "connect" the larger mesopores. The separation between the peak radii of the PSDs for adsorption and desorption pathway increases with the porogen loading, consistent with the increasing hysteresis loop. For the 1% porogen film, the PSD peak radii (albeit a broad peak) for adsorption and desorption both nominally coincide in the 5–6 Å range. For the 30% porogen film the peak pore radius for adsorption occurs at 27 Å while the corresponding desorption peak is at 16 Å.

Despite the approximate nature of the Kelvin equation, the length scales for the PSDs are reasonable. At 34% porosity, a percolated pore structure is expected for the film with 30% porogen loading.[30] The polymeric porogen particles used here are reported to have a radius of 17 Å.[30,31] It is therefore reassuring that the bottleneck of the percolated network obtained from the desorption isotherm is 16 Å, in excellent agreement with the particle size. In general the pore interconnectivity effects (i.e., hysteresis loop) become significant between the porogen loadings of 10–20% (or porosities between 18% and 27% by volume). The peaks in the PSD upon desorption for the 10% and 20% porogen films of 11 and 14 Å are also consistent with a 17 Å porogen particle.

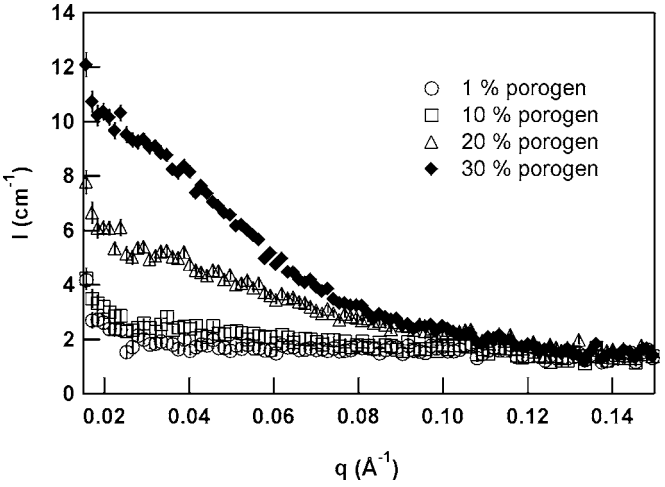

FIG. 6. SANS curves of the porous MSQ films with different porogen loadings. Error bars, sometimes smaller than the size of the data markers, indicate the standard uncertainties in the scattering intensity $I(q)$.

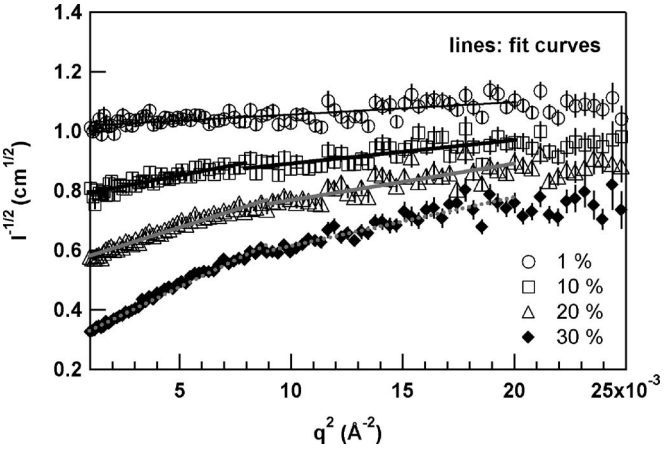

FIG. 7. A plot of $I(q)^{-1/2}$ as a function of q^2 to determine correlation length ξ. The linear fits for each sample that are used to determine the slope and calculate ξ are shown. The data have been vertically offset for clarity and error bars indicate the standard uncertainty.

Slightly smaller bottlenecks would be anticipated if a porous pathway resulted from two porogen particles touching. Turning to the adsorption isotherms, it is striking that some of the larger mesopores in the highly porous samples are actually larger than the size of the porogen particles. If the larger pores are real, aggregation of the porogen particles must occur at the higher loading. To demonstrate that these larger length scales are real, SANS measurements are introduced.

Figure 6 displays the SANS scattering curves as a function of the scattering vector q for the porous MSQ films under vacuum. In this case scattering vector is defined similar to SXR as $q=(4\pi/\lambda)\sin(\theta)$, but in this case λ is the neutron wavelength and 2θ is the scattering angle. The scattering arises from differences in the neutron scattering length density of connecting wall material and the vacuum in the pores, with the scattering of larger pores being more pronounced at lower q. Qualitatively, an increase in the scattering intensity with porogen loading corresponds to the increase in pore size and porosity. The scattering in the film with 1% porogen is too weak to reliably evidence the porosity. This is consistent with the XRP observation that this film contains only 12% of mostly micropores; SANS has difficulty in quantifying pores smaller than 5 Å in diameter, especially at low concentrations. In contrast, the scattering is very strong in the film with 30% porogen, consistent with the larger population of big mesopores.

The SANS data are analyzed quantitatively with a two-phase Debye model to extract an average pore size.[32] In the two-phase Debye model, a random distribution of pore sizes is assumed where the density of the wall material between the pores is uniform. The density correlation function describing the porous structure is assumed to be exponential through $\gamma(r)=\exp(-r/\xi)$, where ξ is the correlation length. The form of the scattered intensity is then given by

$$I(q)=\frac{8\pi P(1-P)\Delta\rho_n^2\xi^3}{(1+q^2\xi^2)^2}, \tag{2}$$

where P is the porosity and $\Delta\rho_n$ is the neutron scattering contrast, a function of ρ_w. To extract correlation length ξ from the SANS curves, Eq. (2) is rearranged into

$$\frac{1}{I(q)^{1/2}}=\frac{1}{(c\xi^3)^{1/2}}+\frac{\xi^2q^2}{(c\xi^3)^{1/2}}, \tag{3}$$

where c is defined as $8\pi P(1-P)\Delta\rho_n^2$. The quantity of ξ can be determined from the slope of $I(q)^{-1/2}$ as a function of q^2, as shown in Fig. 7.

For the film with 1% porogen the plot of $I(q)^{-1/2}$ vs q^2 is linear meaning that a single Debye correlation length is sufficient to describe the structure. However, as the porogen loading increases the curves in Fig. 7 become nonlinear, indicating that the structure is more complex and a single parameter Debye model is insufficient. As typical with SANS/SAXS data only the linear slope at lower q will be used to estimate the dominant pore size. The lines through the experimental data in Fig. 7 indicate the fits used to extract ξ with the lines drawn only through the q range of data included in the fit. Once ξ is known, the P and ρ_w from the XRP data are used to determine the average pore sizes through the equation $l_c=\xi/(1-P)$. As summarized in Table I, the average pore radius from the scattering data at low q increases from 9 to 27 Å as the porogen loading increases from 10% to 30%. These are in good agreement with the peak pore radius obtained from the adsorption isotherms of the XRP data and corroborate the notion of pores larger than the porogen particle. Porogen particle aggregation occurs at higher porogen loadings.

At this point we return to the observation that the pore generating mechanism is not 100% efficient. Additions of 1%, 5%, 10%, 20%, and 30% porogen result in 1%, 4%, 7%, 15%, and 23% porosities. In addition to the possibilities of pore collapse or volatilized porogen not escaping the film, the porogen aggregation phenomenon may also affect the efficacy with which pores are generated. It is conceivable that the interface between the porogen and the MSQ matrix plays a critical role in the pore generation mechanism and this interfacial area will be reduced by porogen aggregation. This seems that reasonable given that the porogen must display partially favorable interactions, i.e., be compatible, with

the MSQ matrix to remain dispersed at moderate loadings. If the porogen did not display compatible interactions with matrix there would be a much stronger propensity for aggregation even at low porogen loadings. This means that the interactions across the porogen/MSQ interface are important and porogen aggregation partially negates these effects. However, additional research is required to perceive the origins of the inefficiencies in the pore generating mechanism in the high porosity samples.

We would be remiss, however, not to discuss the validity of the Kelvin equation in obtaining the PSDs in Fig. 5. It is well known that the simple mechanism of capillary condensation/evaporation is not always appropriate in meso- and microporous materials and that the pore sizes determined from the Kelvin equation may be in error. This is especially problematic for the pores smaller than 10 nm in radius;[33–35] surface forces, not the radius of curvature, are more important for condensation and evaporation mechanisms of such small pores. Despite this fundamental limitation, capillary porosimetry techniques are still widely used in the semiconductor industry[36,37] because the general shape of the adsorption/desorption isotherm provides valuable insights into the pore structure. An example is Fig. 4 where a wealth of information, both qualitative and quantitative, was obtained before Eq. (1) was ever invoked. Furthermore the total porosity and wall density do not invoke the mechanism of capillary condensation. More complex models, which are based on corrections to the Kelvin equation, have been developed to describe the pore filling of mesoporous materials.[38,39] Even with these additional parameters, quantitative estimates of the PSD can be more than 100% in error for pores less than 10 nm in radius, and none of the existing interpretations of capillary condensation yield reliable pore sizes.[33–35] More accurate interpretations require computer modeling and/or simulations of the isotherms such as Gage cell Monte Carlo (GCMC) simulations or nonlinear density functional theory (NLDFT) methods. Given these constraints, the Kelvin equation in its simplest form has been used to provide a qualitative estimate of the PSD for these materials. Instead of choosing more complex model (still with potential errors to characterize pore structures) and developing computer simulation model, we utilize complimentary measurement techniques such as SANS to corroborate the XRP data. Surprisingly, the PSD extracted from the XRP measurements makes physical sense in terms of both the porogen particle size and the corroborating SANS data. However, this may not always be the case. It is always prudent to combine several techniques to determine the most accurate structural characteristics in these porous low-k dielectric films.

SUMMARY

We have applied xray porosimetry and SANS to characterize the average film density, matrix material density, porosity, and pore size distributions of MSQ based porous low-k thin films with varying porogen contents. The combination of these techniques provides highly complimentary pore structure information. It appears that the native MSQ resin contains approximately 11% volume porosity of micropores. As the porogen content increases, both the pore size and porosity increase and the average density decreases, while wall density remains unchanged. However, the conversion of porogen to pore was less than 100% efficient. It is not clear if this is due to the collapse of small pores at elevated temperatures, porogen residue becoming entrapped in the film, or porogen particle aggregation at high porosities. The pore sizes determined from adsorption and desorption isotherms of XRP were compared to those from SANS. Generally, the average pore sizes increase as with the porogen loading. At high porogen loading the "bottleneck" effect from the hysteresis loop was used to deduce an interconnected distribution of pore sizes with access to the larger pores being dictated through the smaller pores. For films with 10%, 20%, and 30% porogen both SANS and XRP confirm that these larger pores were on the order of 10, 17, and 27 Å, respectively. For films with less than 10% porogen, the interconnectivity effects were not observed and the porosity was dominated by the intrinsic porosity of the MSQ matrix.

ACKNOWLEDGMENTS

We acknowledge the support of the National Institute of Standards and Technology, U.S. Department of Commerce, in providing the neutron research facilities used in this work. The experimental assistance on the 8 m SANS line from Derek Ho and Charles Glinka (NCNR) is also appreciated.

[1] C. J. Hawker, J. L. Hedrick, R. D. Miller, and W. Volksen, MRS Bull. **25**, 54 (2000).
[2] E. Kondoh, T. Asano, A. Nakashima, and M. Komatu, J. Vac. Sci. Technol. B **18**, 1276 (2000).
[3] S. Mikoshiba and S. Hayase, J. Mater. Chem. **9**, 591 (1999).
[4] H. S. Yang, S. Y. Choi, S. H. Hyun, and C. G. Park, Thin Solid Films **348**, 69 (1999).
[5] S. Yang *et al.*, Chem. Mater. **13**, 2762 (2001).
[6] A. Grill, J. Appl. Phys. **93**, 1785 (2003).
[7] Q. R. Huang, W. Volksen, E. Huang, M. C. Toney, W. Frank, and R. D. Miller, Chem. Mater. **14**, 3676 (2002).
[8] J. J. Si, H. Ono, K. Uchida, S. Nozaki, H. Morisaki, and N. Itoh, Appl. Phys. Lett. **79**, 3140 (2001).
[9] Z. Wang, A. Mitra, H. Wang, L. Huang, and Y. Yan, Adv. Mater. (Weinheim, Ger.) **13**, 1463 (2001).
[10] International Technology Roadmap for Semiconductor (ITRS), 2004 (website: http://www.itrs.net/Common/2004Update/2004_00_Overview.pdf).
[11] M. Mosig, T. Jacobs, K. Brennan, M. Rasco, J. Wolf, and R. Augur, Microelectron. Eng. **64**, 11 (2002).
[12] *Sol-Gel Technology for Thin Films, Fibers, Preforms, Electronics, and Speciality Shapes*, edited by L. C. Klein (Noyes, Park Ridge, NJ, 1988).
[13] H. Yanazawa, H. Mastunaga, H. Itoh, K. Nakai, and I. Suzuki, J. Vac. Sci. Technol. B **20**, 1833 (2000).
[14] D. W. Gidley, W. E. Frieze, T. L. Dull, A. F. Yee, C. V. Nguyen, and D. Y. Yoon, Appl. Phys. Lett. **76**, 1282 (2000).
[15] C. L. Wang, M. H. Weber, K. G. Lynn, and K. P. Rodbell, Appl. Phys. Lett. **81**, 4413 (2002).
[16] M. R. Baklanov, K. P. Mogilnikov, V. G. Polovinkin, and F. N. Dultsev, J. Vac. Sci. Technol. B **18**, 1385 (2000).
[17] K. Omoto, Y. Ito, and S. Kawamura, Appl. Phys. Lett. **82**, 544 (2003).
[18] W. L. Wu, W. E. Wallace, E. K. Lin, G. W. Lynn, C. J. Glinka, E. T. Ryan, and H. M. Ho, J. Appl. Phys. **87**, 1193 (2000).
[19] H. J. Lee, C. L. Soles, W. W. Liu, B. J. Bauer, and W. L. Wu, J. Polym. Sci., Part B: Polym. Phys. **40**, 2170 (2002).
[20] H. J. Lee, E. K. Lin, B. J. Bauer, W. L. Wu, B. K. Hwang, and W. D. Gray, Appl. Phys. Lett. **82**, 1084 (2003).
[21] M. Gallagher *et al.*, presented at MRS Spring Meeting, San Francisco, 2001 (unpublished).

[22]M. Gallagher *et al.*, Proceedings of American Chemical Society (ACS), 87, 442 (2002).
[23]J. R. Tesmer and M. Nastasi, *Handbook of Modern Ion Beam Materials Analysis* (Materials Research Society, Pittsburgh, 1995).
[24]The data throughout the manuscript and in the figures are presented along with the standard uncertainty (±) involved in the measurement.
[25]L. G. Parratt, Phys. Rev. **95**, 359 (1954).
[26]J. Bolze, M. Ree, H. S. Youn, S. H. Chu, and K. Char, Langmuir **17**, 6683 (2001).
[27]M. Kruk and M. Jaroniec, Chem. Mater. **13**, 3169 (2001).
[28]K. S. W. Sing, D. H. Everett, R. A. W. Haul, L. Moscou, R. A. Pierotti, J. Rouquerol, and T. Siemieniewska, Pure Appl. Chem. **57**, 603 (1985).
[29]E. O. Kraemer, *A Treatise on Physical Chemistry*, edited by H. S. Taylor (Macmillan, New York, 1931), p. 1661.
[30]M. R. Baklanov *et al.*, Proceedings of Advanced Metallization Conference (AMC), 271 (2002)
[31]C. M. Flannery, T. Wittkowski, K. Jung, B. Hilebrands, and M. R. Baklanov, Appl. Phys. Lett. **80**, 4594 (2002).
[32]P. Debye, H. R. Anderson, and H. Brumberger, J. Appl. Phys. **28**, 679 (1957).
[33]A. Neimark, P. I. Ravikovitch, and A. Vishnyakov, Phys. Rev. E **62**, R1493 (2000).
[34]A. V. Neimark, F. Schuth, and K. K. Unger, Langmuir **11**, 4765 (1995).
[35]P. I. Ravikovitch, A. Vishnyakov, and A. Neimark, Phys. Rev. E **64**, 011602 (2001).
[36]A. Grill, V. Patel, K. P. Rodbell, E. Huang, M. R. Baklanov, K. P. Mogilnikov, M. Toney, and H.-C. Kim, J. Appl. Phys. **94**, 3427 (2003).
[37]M. R. Baklanov and K. P. Mogilnikov, Microelectron. Eng. **64**, 335 (2002).
[38]E. P. Barrett, L. G. Joyner, and P. H. Halenda, J. Am. Chem. Soc. **73**, 373 (1951).
[39]J. C. P. Broekhoff and J. de Boer J. Catal. **9**, 8 (1967).